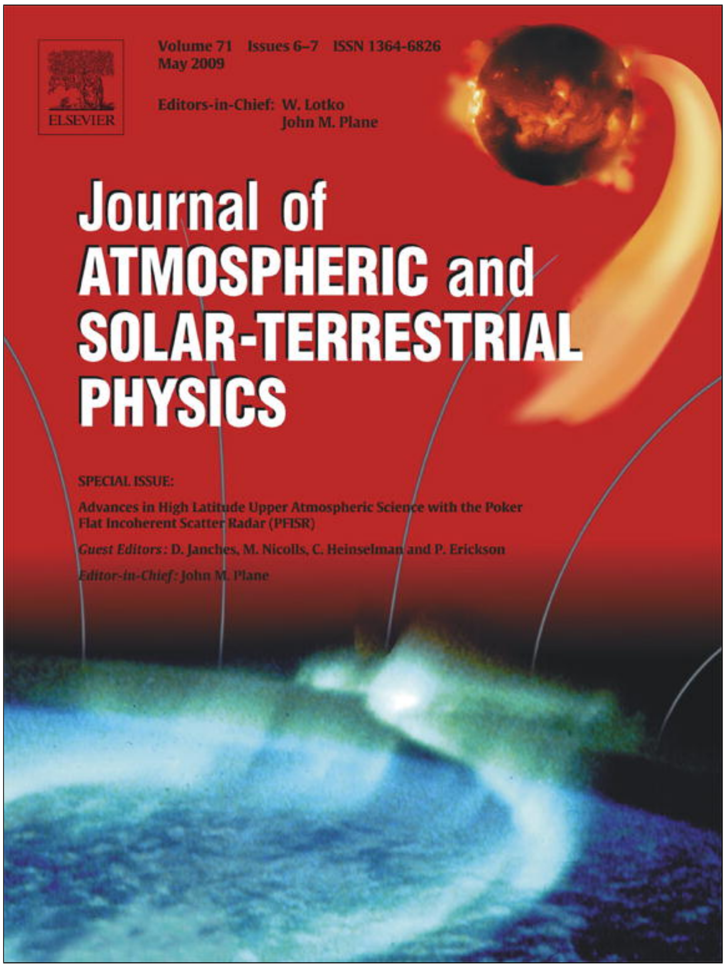
ELSEVIER
Volume 71 Issues 6–7 ISSN 1364-6826
May 2009
Editors-in-Chief: W. Lotko
John M. Plane
Journal of
ATMOSPHERIC and
SOLAR-TERRESTRIAL
PHYSICS
SPECIAL ISSUE:
Advances in High Latitude Upper Atmospheric Science with the Poker Flat Incoherent Scatter Radar (PFISR)
Guest Editors: D. Janches, M. Nicolls, C. Heinselman and P. Erickson
Editor-in-Chief: John M. Plane

Journal of Atmospheric and Solar-Terrestrial Physics 71 (2009) 675–687

Contents lists available at ScienceDirect

Journal of Atmospheric and Solar-Terrestrial Physics

journal homepage: www.elsevier.com/locate/jastp

Coordinated optical and radar image measurements of noctilucent clouds and polar mesospheric summer echoes

M.J. Taylor [a], Y. Zhao [a,*], P.-D. Pautet [a], M.J. Nicolls [b], R.L. Collins [c], J. Barker-Tvedtnes [a], C.D. Burton [a], B. Thurairajah [c], J. Reimuller [d], R.H. Varney [e], C.J. Heinselman [b], K. Mizutani [f]

[a] Center for Atmospheric and Space Sciences, Utah State University, Logan, UT, USA
[b] Center for Geospace Studies, SRI International, Menlo Park, CA, USA
[c] Geophysical Institute, University of Alaska, Fairbanks, AK, USA
[d] Department of Aerospace Engineering Sciences, University of Colorado, Boulder, CO, USA
[e] Department of Electrical and Computer Engineering, Cornell University, Ithaca, NY, USA
[f] Environment Sensing and Network Group, National Institute of Information and Communications Technology, Tokyo, Japan

A R T I C L E I N F O

Article history:
Received 13 May 2008
Received in revised form
19 September 2008
Accepted 12 December 2008
Available online 6 January 2009

Keywords:
Noctilucent clouds (NLC)
Polar mesosphere summer echoes (PMSE)
Ploar mesospheric clouds (PMC)
High-latitude summer mesosphere

A B S T R A C T

Novel coincident 3-D radar, lidar and optical image measurements of dynamical structures in polar mesosphere summer echoes (PMSE) and noctilucent clouds (NLC) are presented. Common volume mesospheric measurements were made over central Alaska using the new Poker Flat Incoherent Scatter Radar (PFISR), a co-located Rayleigh lidar and remote, two-station digital image observations, enabling the first detailed investigation of the horizontal and vertical structures of NLC and PMSE. Coincident measurements were made of an unusual NLC display recorded on 10–11 August 2007, characterized by a broad luminous band that contained several prominent wave forms. Concurrent lidar and image measurements established the presence of NLC within the radar volume from ~09:00 UT (01:00 LT), when the solar depression angle was 10.4°, until dawn. Strong but intermittent PMSE were detected by PFISR, with distinct patchy structures that exhibited a similar southward motion as the NLC. Detailed comparison of the 3-D PMSE structures and the NLC lidar and image data have revealed striking similarities when account was taken of the NLC layer altitude, suggesting a direct link between their small-scale spatial signatures (within the current resolution of the radar measurements). At the same time, the lidar detected a sustained increase in the backscatter signal, while the imagers revealed the development of copious short horizontal wavelength (4.9 km) billow waves. We conclude that strong wind shears associated with the Kelvin–Helmholtz billow instabilities played a key role in the development of a neutral turbulence layer in close proximity to the NLC layer resulting in the strong but intermittent PMSE detected at 450 MHz on this occasion.

1. Introduction

Noctilucent clouds (NLC) are well-established, high-latitude mesospheric phenomena that are visible to the naked eye, with initial reports extending back in time over 100 years (Backhouse, 1885; Leslie, 1885). Subsequent ground-based and rocket-borne measurements have determined their remarkably consistent altitude, occurring in the upper mesosphere at a mean height of ~83 km (e.g. Jesse, 1896; Strörmer, 1933; Paton, 1964; Grahn and Witt, 1971; Witt et al., 1971; Bjorn et al., 1985; Taylor et al., 1984, Gadsden and Taylor, 1994, von Zahn et al., 1998; Chu et al., 2001; Collins et al., 2003; Thayer et al., 2003; Fiedler et al., 2005; Gerding et al., 2007). NLC are seasonal, appearing during the summer months in close association with the observed rapid decrease in mesopause temperatures that result from strong upwelling in the summer polar region in response to the gravity wave-driven mean meridional circulation (e.g. Lübken, 1999; Fritts and Alexander, 2003). At these cold mesopause temperatures (typically 130 K), microscopic ice crystals can nucleate and grow to observable sizes (typically 40 nm diameter), over periods of several hours to a few days, when they become visible as NLC (Gadsden, 1981; Jensen and Thomas, 1988; Rapp and Thomas, 2006).

From the ground, NLC are seen by strong forward scattering of sunlight from the ice particles, often appearing as an extensive cloud layer with a distinct lower border at ~83 km (e.g. Witt, 1962; Grahn and Witt, 1971; Taylor et al., 1984). The clouds are conspicuous by their silvery blue color and are usually characterized by a variety of structures including gravity wave bands and billows (e.g. Fogle and Haurwitz, 1969; Gadsden and Schröder,

* Corresponding author. Tel.: +1 435 7978128.
E-mail address: yucheng@cc.usu.edu (Y. Zhao).

1364-6826/$ - see front matter © 2009 Elsevier Ltd. All rights reserved.
doi:10.1016/j.jastp.2008.12.005

1989). However, due to their tenuous nature, NLC are only visible to the eye during the hours of twilight when the observer and the atmosphere below are in darkness, while the clouds themselves remain sunlit (this situation occurs for solar depression angles ~6–16°). Visible observations over the past century have established the best observing conditions occur over the latitude range ~50–65°, and have provided important information on NLC occurrence, morphology and latitudinal extent (e.g. Gadsden, 1998; Gadsden and Schröder, 1989).

Satellite observations, aptly termed polar mesospheric clouds (PMC), have revolutionized our understanding of these mesospheric clouds and their spatial and temporal variability. From their earliest measurements by the OGO-6 satellite (Donahue et al., 1972), and by the Solar Mesosphere Explorer (SME) satellite (Thomas, 1984), these measurements have established the near continuous presence of a PMC layer in the perpetually sunlit summer polar regions over the Arctic (May–August) and Antarctic (November-February), where ground-based measurements are very limited (e.g., Jensen et al., 1988; Thomas et al., 1991; Evans et al., 1995; Carbary et al., 2000; von Savigny and Burrows, 2007; Bailey et al., 2005; Russell III et al., 2009). Most importantly, satellite measurements have provided a consistent measure of PMC occurrence, latitudinal extent, and brightness. As a result, the 30-year long series of measurements by the SBUV instrument on the NOAA satellite series have recently provided persuasive evidence that PMC are increasing in their frequency of occurrence and brightness over the past 30 years (Deland et al., 2006). In parallel, ground-based observations of NLC suggest an increase in the number of cloud sightings at significantly lower-latitudes than previously reported (e.g., Taylor et al., 2002; Zalcik, 1998) prompting speculation concerning long-term change in the mesospheric environment (e.g. Thomas et al., 1989; von Zahn, 2003).

With the advent of lidar systems, a powerful new ground-based instrument became available to probe the NLC layer (Hansen et al., 1989). Lidar observations provide unique data on the NLC height, thickness, and backscatter strength, with good local time coverage, that can complement satellite observations. Lidar measurements of NLC have now been made from a number of high-latitude sites in both the Arctic and Antarctic regions and often show a continuous layer of a few km thickness modulated by gravity waves and tides (e.g. von Zahn et al., 1998; Chu et al., 2001; Collins et al., 2003; Thayer et al., 2003; Fiedler et al., 2005; Gerding et al., 2007). In particular, the combination of lidar and NLC image measurements has demonstrated the advantage of investigating NLC and their temporal and spatial properties (e.g. Wickwar et al., 2002; Collins et al., 2009).

In the late 1970s, a new mesospheric phenomena was discovered (Czechowsky et al., 1979). Polar mesosphere summer echoes (PMSE) are intense radar echoes with some of the first detections observed using a 50 MHz VHF radar operated at the Poker Flat Research Range (PFRR), in central Alaska (Ecklund and Balsley, 1981). PMSE are now known to be closely associated with NLC. They exhibit very similar seasonal and geographical occurrence (e.g. Jensen et al., 1988; Lübken et al., 1995; Cho and Röttger, 1997; Hoffmann et al., 1999; Rapp and Lübken, 2004). Detailed investigations using radar, lidar, and coordinated rocket-borne measurements have established a clear relationship between PMSE and NLC, with the PMSE often occurring in a layer immediately above (and sometimes overlapping) the NLC layer (mean PMSE layer ~2–3 km above the NLC layer) (e.g. Nussbaumer et al., 1996; von Zahn and Bremer, 1999). The PMSE and NLC often exhibit common altitudinal variability and wave-like structures (e.g. Ruster et al., 1996; Ruster, 1997; Czechowsky and Ruster, 1997; Chilson et al., 2001). However, this is not always the case and PMSE have been detected in the absence of NLC (and vice versa). Attempts to determine a correlation between PMSE and NLC image data have been less successful, revealing at best only a weak correlation (Taylor et al., 1989; Kirkwood et al., 1995).

PMSE are coherent backscatter returns from irregularities in the radar refractive index most likely induced by turbulence (e.g., Cho et al., 1992; Rapp and Lübken, 2003). At mesopause altitudes the refractive index variations are determined primarily by the electron density and for efficient scattering, the electron density structures need to have scales of half the radar wavelength (~3 m at VHF), known as the Bragg condition (Tatarskii, 1961). Detailed measurements and modeling studies (e.g., Rapp and Lübken, 2004) have shown that PMSE are most probably associated with an enhancement of electron diffusion rate over that of kinematic viscosity (enhancement of the so-called Schmidt number) due mainly to the presence of sub-visible ice particles of smaller size (~10–20 nm) that typically reside in the growth region between the mesopause and the region immediately above the NLC layer. These ice/aerosol particles exist in the D-region ionosphere and are thought to become negatively charged by electron attachment at the ice surface. Turbulent motions in the neutral atmosphere generated by gravity wave breaking, and in-situ instability processes, cause small-scale structures in the distribution of the charged ice particles which create irregularities in the refractive index that are observed as PMSE (e.g., Cho and Röttger, 1997; Fritts et al., 2003; Rapp and Lübken, 2004; Rapp et al., 2008). However, PMSE can also be produced by larger particles responsible for visible NLC (typically >40 nm radius), and can therefore occur within the NLC layer (e.g., Rapp et al., 2008). Thus, both PMSE and NLC are linked together usually by different parts of the ice particle distribution, but with PMSE highly sensitive to background ionospheric parameters (electron density, electron density gradients, etc.) and to neutral motions and turbulence.

Most PMSE measurements have been made with VHF radar systems at probing angles close to the zenith (e.g. Balsley et al., 1983; Hoffmann et al., 2005). Observations at VHF are more prevalent than at other frequencies because the radar backscattering cross-section for PMSE reduces significantly with increasing frequency, over 6 orders of magnitude from 50 to 500 MHz (Rapp and Lübken, 2004). The radar backscatter signal has also been shown to be highly aspect sensitive with maximum signal near the zenith (Czechowsky et al., 1988; Chilson et al., 2002). PMSE have been detected at higher frequencies, mainly using the EISCAT 224 MHz system (e.g. Hoppe et al., 1988; Röttger and La Hoz, 1990), and the 933 MHz system in northern Scandinavia (e.g. La Hoz et al., 2006; Rapp et al., 2008). One detection exists at 1.29 GHz using the Sondrestrom incoherent scatter radar in Greenland (Cho and Kelley, 1992).

Recent measurements using the new PFISR phased array have demonstrated its capability to detect PMSE at 450 MHz and have provided the first 2-D horizontal structure of PMSE as a function of altitude (Nicolls et al., 2009). Another paper in this special issue focuses on the spectral properties of PMSE measured by PFISR (Nicolls et al., 2009). Here we utilize this new radar capability to investigate NLC and PMSE common volume dynamics using simultaneous optical imaging, lidar, and PFISR measurements at the PFRR. The measurements were performed in conjunction with the NASA Aeronomy of Ice in the Mesosphere (AIM) satellite mission. Our primary goal was to quantify NLC occurrence and horizontal and vertical structure over PFRR at the same time that PFISR measured the horizontal spatial characteristics and altitudinal variability of PMSE.

2. Instrumentation

Three sets of ground-based instruments were used in this coordinated study of NLC and PMSE over central Alaska.

2.1. The Poker Flat Incoherent Scatter Radar (PFISR)

PFISR is a powerful new incoherent scatter radar developed for the National Science Foundation by SRI International. A key feature of PFISR is its phased array technology that enables rapid steering of the radar beam, on a pulse-to-pulse basis, creating detailed two- and 3-D mappings of a broad range of phenomena in the high-latitude ionized upper atmosphere. The radar was recently deployed at Poker Flat Research Range (65.13°N, 147.47°W) near Fairbanks, Alaska, and the first UHF measurements of PMSE at 450 MHz were made during the early summer of 2007 (Nicolls et al., 2007). The radar has a beam-width of $\sim 1^\circ$ and is mounted on a tilted platform to enable measurements of the high-elevation sky to the north of PFRR, including the magnetic zenith (towards the south). Fig. 1 maps the relative locations of the 26 radar beams employed by PFISR for this coordinated NLC and PMSE measurements program. Twenty-five of the beams formed a $5^\circ \times 5^\circ$ rectangular array (centered on the bore-sight direction), that extended from the zenith down to $\sim 55^\circ$ elevation. The 26th beam looked up the magnetic field line at PFRR. The array was rotated $\sim 15^\circ$ east of north and encompassed a $\sim 65 \times 65$ km area at PMSE altitudes (~ 85 km). As the beams are separated by ~ 15 km at PMSE altitudes, smaller-scale structures cannot be resolved with this experiment configuration. Beam 23 was aimed vertically for direct comparison with the Rayleigh lidar NLC backscatter measurements. The operational mode was similar to that employed by Nicolls et al. (2007) to image PMSE structure at UHF and consisted of transmitting 10 μs (1.5 km), 13-baud Barker-coded pulses on two frequencies (449.6 and 449.3 MHz) to best utilize the available duty cycle of the system ($\sim 10\%$). The peak power during this experiment was approximately 1.3 MW. The data were integrated online for 16 s, corresponding to ~ 128 pulses per direction, per frequency. In this imaging mode, no Doppler (spectral) information is available.

2.2. Rayleigh lidar

The National Institute of Information and Communications Technology (NICT) Rayleigh lidar has operated at PFRR since 1998 as part of a collaborative program to investigate the polar neutral upper atmosphere including the occurrence and properties of NLC over central Alaska during the summer months. Details of the lidar and its operation are given in Mizutani et al. (2000) and Collins et al. (2003), and only the main points are presented here. Briefly, the lidar system utilized a Nd:YAG laser and a 0.6 m receiving telescope. The laser has an average power of 8 W and was operated at 532 nm with a pulse repetition rate of 20 Hz and a pulse width of 7 ns (full-width half-maximum, FWHM). The field-of-view of the receiver telescope was 1 mrad and the optical bandwidth was 0.3 nm, FWHM. The returned photons were integrated over 0.5 s yielding a 75 m range sampling resolution. The raw data were then integrated for 1000 pulses (~ 50 s) and the profiles smoothed using a running average of 0.225 km, integrated over 200 s. In this study, we utilize the backscatter coefficient data to characterize the strength and altitudinal variability of NLC present in the zenith over PFRR (e.g. Collins et al., 2009).

2.2.1. Two-station digital imaging

To investigate the 2-D spatial and temporal properties of NLC in the lidar and radar sample volumes, two optical sites were set up to the southeast of PFRR; one at Donnelly Dome (63.8°N, 145.8°W) and the other at Gerstle River (63.8°N, 144.9°W) at ground ranges of ~ 166.5 and 189.0 km, respectively from PFRR.

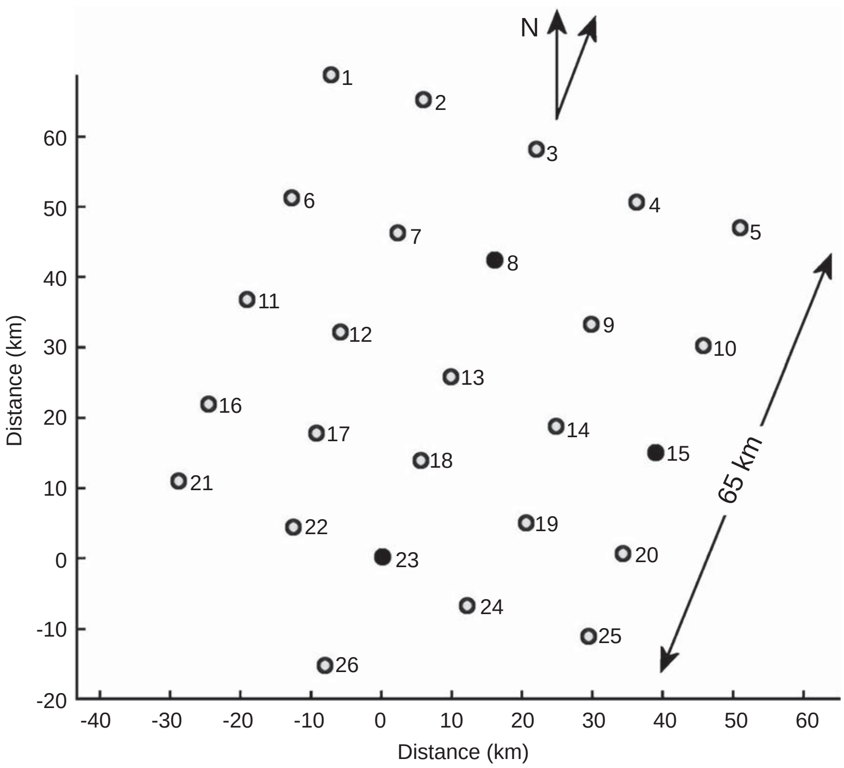

Fig. 1. Map showing the relative locations of the 26 radar beams used by PFISR for the PMSE image measurements projected onto the 85 km level. Twenty-five of the beams formed a 5×5 rectangular array with beam 23 pointing vertically for coincident measurements with the lidar.

Both sites provided superior viewing of NLC within the northern twilight sky. Donnelly Dome has been utilized previously during August 2005 to study NLC in coordination with Rayleigh lidar measurements at PFRR (Collins et al., 2009). Gerstle River provided a second location ~43.3 km to the ~East of Donnelly Dome, enabling a two-station parallel axis-imaging capability for investigating the spatial properties of the NLC structures. Coincident measurements from these two sites also provided an important redundancy to help mitigate problems due to the highly variable local weather conditions. High-resolution digital images of NLC were obtained at 30 s intervals (synchronized to the minute) from both sites using two computer-controlled Canon D5 SLR cameras fitted with Canon EF 28–135 mm zoom lenses, each operated with a field of view of 40° horizontal by 30° vertical. The cameras were aimed at ~15° elevation to the ~NW horizon and centered on the PFRR azimuth.

Fig. 2 illustrates the observing geometry for the different instruments. The field of view of each camera is plotted for 5–30° elevation assuming a mean NLC altitude of 82.5 km. This region encompassed the lidar and radar measurements at PFRR and extended several hundred kilometers further to the NW to record and characterize NLC structure and occurrence. In this configuration, PFRR is near the top of the cameras' field of view, while the PFISR footprint, indicated by the rectangular box, is also in the near field of the NLC image measurements. Ideally, the coincident volume should have been closer to the center of the cameras' fields of view. However, the two camera sites were chosen for their accessibility and generally good viewing conditions, and were located immediately north of the Alaska Range. Each image was tagged with UT time (accurate to 1 s) and the elevation and azimuth of the cameras were set using the local star field and previously measured horizon markers. In addition to the two-station digital image measurements, color video recordings were made from both sites using two Sony DCR-VX2100 camcorders (with low-light level capability), to help document the evolution of the NLC displays. Wide angle (70° × 50°) panoramic images of the NLC were also taken from Donnelly Dome using a Fuji FinePix S Pro SLR camera equipped with a 16 mm (F/5.6) lens system. For this study the NLC image data were first calibrated using the star background and then mapped into geographic coordinates, assuming a cloud altitude of 82.5 km, for direct comparison with the radar and lidar data.

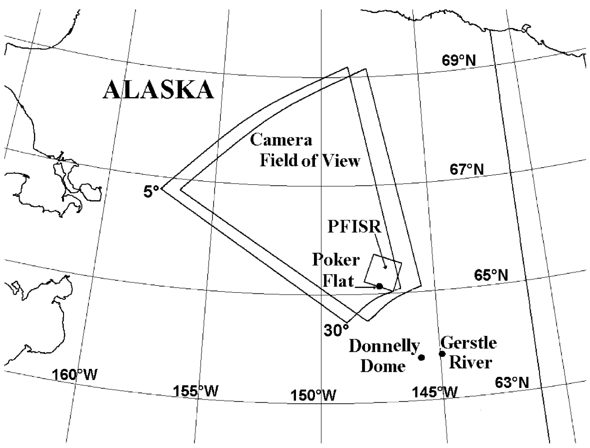

Fig. 2. Sketch showing the observing geometry for the different instruments. The lidar operated in the zenith from PFRR while the box shows the PFISR field of view. NLC image measurements were made from Donnelly Dome and Gerstle River to the ~SE of PFRR. The field of view of each camera is plotted for 5–30° elevation, assuming an NLC altitude of 82.5 km. This region encompassed the lidar and radar measurements at PFRR and extended several hundred kilometers to the NW to characterize the NLC structure.

3. Observations and results 10/11 August

Joint optical and radar observations were made over the period 27 July–15 August when the solar depression angle (SDA) was > 6° suitable for viewing NLC against the bright twilit sky (e.g. Gadsden and Schröder, 1989). PFISR observations were scheduled from 27–31 July and 8–15 August, from 06 to 11 UT (22:00–3:00 LT) where LT = UT−8 h. PMSE was first observed by PFISR beginning late May of 2007 (Varney et al., 2009) and intermittently throughout the summer, with a low occurrence rate (just a few percent) (Varney et al., 2009). The intermittency is at least partly caused by the necessary D-region ionization for enhancement of the backscatter cross-section (Rapp et al., 2002), but is mainly due to the high probing frequency (small Bragg wavelength) of PFISR. Much of observed PMSE at these high frequencies is thought to be associated with fossilized structures, that once created, are advected through the observing volume (Nicolls et al., 2007), possibly eliminating the necessity for concurrent active neutral air turbulence (Rapp and Lübken, 2003) (although the duration of some echoes, which often persist for tens of minutes, are still difficult to explain under this scenario (e.g., La Hoz et al., 2006; Nicolls et al., 2009), as diffusion times are expected to be some tens of seconds at UHF). Owing to the necessary D-region densities (of at least $\sim 10^9\,\mathrm{m}^{-3}$ (Rapp et al., 2002), and possibly higher at UHF), nighttime observations of PMSE tend to occur during periods of aurorally induced ionization (e.g. Janches et al., 2009; Varney et al., 2009). On the night of 10/11 August there was considerable auroral activity accompanied by a sporadic E layer, and the radar recorded the effects of fairly constant (in time) auroral precipitation down to 90–95 km. The skies were mainly clear and a well-developed NLC display was observed visually for over 4 h, with 3 h of coincident lidar measurements and 2 h of radar PMSE measurements. Indeed, the lidar operators at PFRR later noted that this event developed into one of the most striking NLC displays that they had seen in the past several years. Simultaneous lidar, radar and image data were obtained from all stations during the latter part of the night from ~09:00–11:00 UT (01:00–03:00 LT).

The lidar and two-station image measurements started at twilight around 07:40 UT (23:40 LT) when the SDA was ~7° and continued until dawn ~12:20 UT. NLC were first detected at both imager sites around ~08:00 UT (00:00 LT). The display was initially characterized by a single faint curved band with some limited filament structure at low-elevations. In particular, there was no visual evidence for NLC at higher elevations. Subsequent time-lapse analysis of the image data (not shown) indicates that the NLC display was developing to the north and moving southwards. The lidar revealed no evidence of NLC overhead at PFRR at this time and PFISR observations, which started earlier at 06:00 UT, showed no PMSE. This situation changed dramatically around 09:00 UT when both the lidar and radar suddenly detected significant mesospheric echoes. At the same time the Donnelly Dome image data clearly showed a large patch of NLC extend to higher elevations overhead at PFRR. Thereafter, the lidar observations established the presence of a continuous NLC layer until 11:00 UT, while the radar detected intermittent PMSE that developed significantly in strength and structure around 10:00–11:00 UT. After 11:00 UT the radar was switched to a spectral observing mode where the PMSE was observed to weaken and diffuse away. The continued observations of PMSE later during this day (11th August) are reported in Nicolls et al. (2009). For this study, we focus on coincident measurement period (09:00–11:00 UT) when NLC were clearly imaged in the lidar and radar common volume.

Fig. 3a shows an example image of the NLC display recorded approximately 2 h after NLC were first sighted. The data were taken from Gerstle River (at 10:10 UT) when the SDA was ~10.6° and shortly before strong PMSE were detected by PFISR.

By this time, the visible NLC display had developed significantly and was now characterized by a large broad luminous band that stretched across the cameras field of view and contained many bright wave forms with some smaller-scale billows. This prominent feature was observed to move almost due southwards over the next hour. Fig. 3b shows a map of this NLC image projected onto a geographic grid assuming a cloud layer altitude of 82.5 km. The NLC data have also been flat-fielded, using a background sky image, to enhance the visibility of the cloud structures. The broad NLC band is unmistakable, extending almost east–west at this time, but exhibiting some curvature towards the north–west. Fainter NLC structures are also evident extending out of this bright region into the PFISR sample volume (see Section 4).

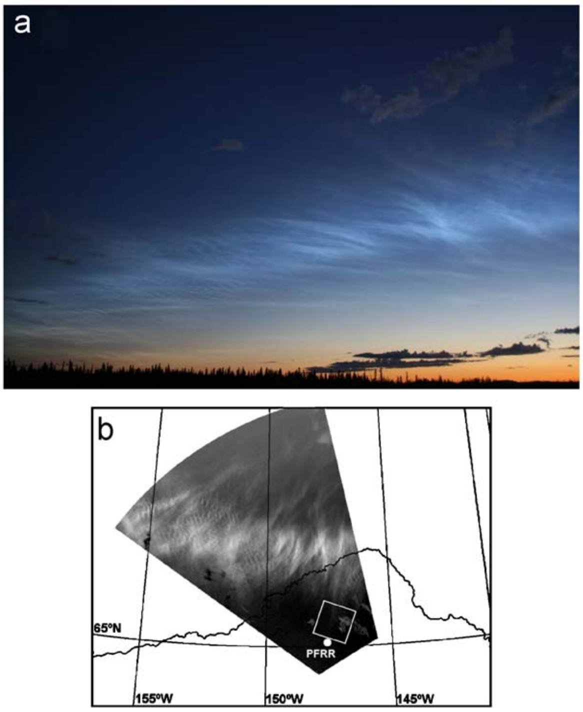

Fig. 3. (a) Example image of the NLC display recorded on 10–11 August from Gerstle River at 10:10 UT (02:10 LT). At this time the NLC were characterized by a broad luminous band that stretched across the camera field of view and contained many wave forms, including smaller-scale billows. (b) Map of NLC projected onto a geographic grid assuming a layer altitude of 82.5 km. The data have been flat-fielded using a background sky image to enhance the visibility of the NLC structures.

Fig. 4 charts the subsequent development of the NLC display over a ~30 min interval (10:25–10:53 UT) when the PMSE signals strengthened significantly. As with Fig. 3b, the image data were flat-fielded to enhance the presentation of the NLC structures. During this interval the broad luminous band of NLC moved overhead at PFRR, with concurrent large increases in the lidar backscatter and radar PMSE (discussed in detail later). By 10:45 UT the visual NLC display had evolved and expanded in area to almost fill the camera's field of view and was dominated by extensive billow-type patterns.

Fig. 5 summarizes the lidar backscatter coefficient measurements that were obtained from 07:30 to 12:25 UT (23:30–04:25 LT). The data are plotted on a log scale to emphasize the NLC structures. As discussed earlier, no NLC were detected by the lidar for the first ~1.5 h of observations. However, at ~09:00 UT (01:00 LT), NLC were suddenly detected overhead at PFRR coinciding with the intrusion of leading structures from the extensive NLC band as it approached PFRR. Thereafter, the lidar data clearly established the presence of a well-developed NLC layer in the zenith that varied significantly in height and strength during the rest of the night (~3 h period). Initially, the NLC layer was centered at ~83.5 km and exhibited an apparent thickness of ~1.5 km. Over the next 30 min, the NLC layer increased systematically in altitude to ~84.5 km. During the following hour, the layer descended back down to ~83.5 km, while at the same time the integrated backscatter coefficient increased by a factor of ~4 from 2.5×10^{-7} to $1.0 \times 10^{-6}\,\mathrm{sr}^{-1}$. Detailed examination of the lidar signal during this interval indicates evidence of layering structure within the NLC, starting around 10:15 UT and becoming

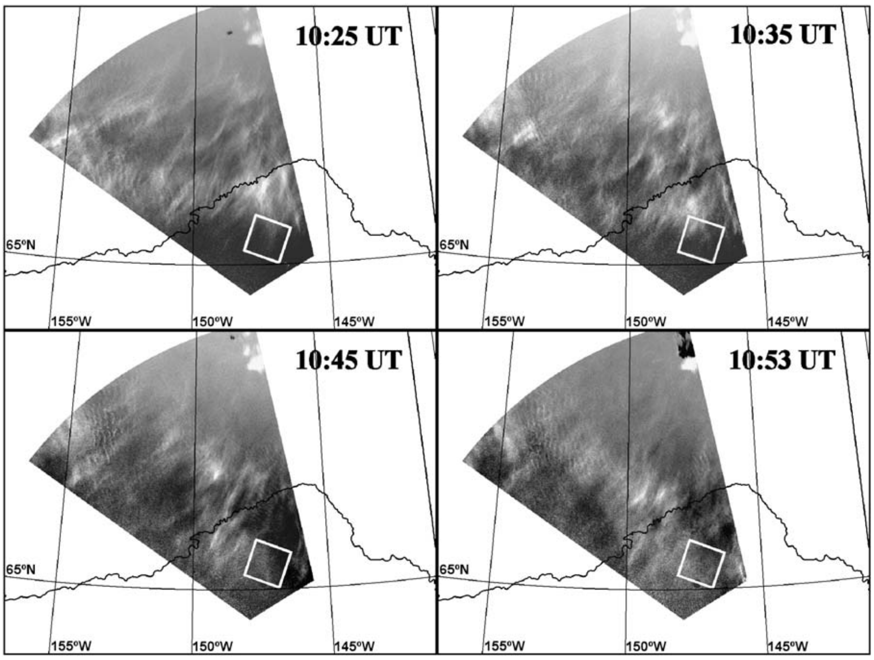

Fig. 4. NLC maps charting the motion and development of NLC display at 10 min intervals (from 10:25 UT) during intermittent PMSE. The white box indicates the PFISR field of view.

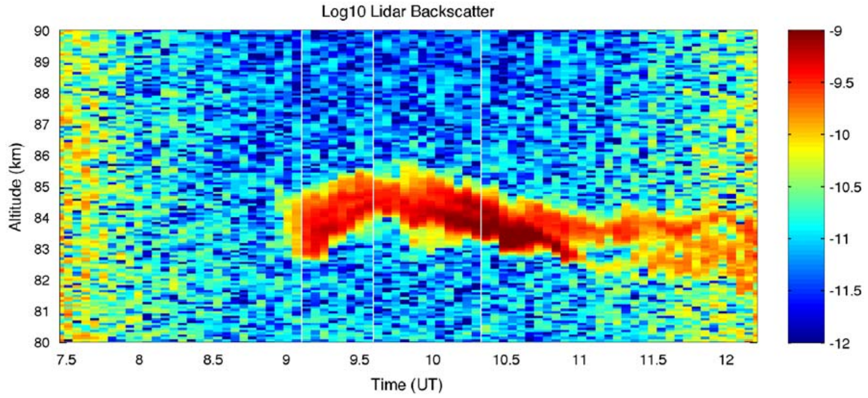

Fig. 5. Summary plot of the lidar backscatter coefficient data (logarithmic scale) for 10/11 August. Initially, no NLC detected. After ~9:00 UT, the lidar measured a continuous NLC layer that appeared to divide into two less distinct layers after 11:00 UT.

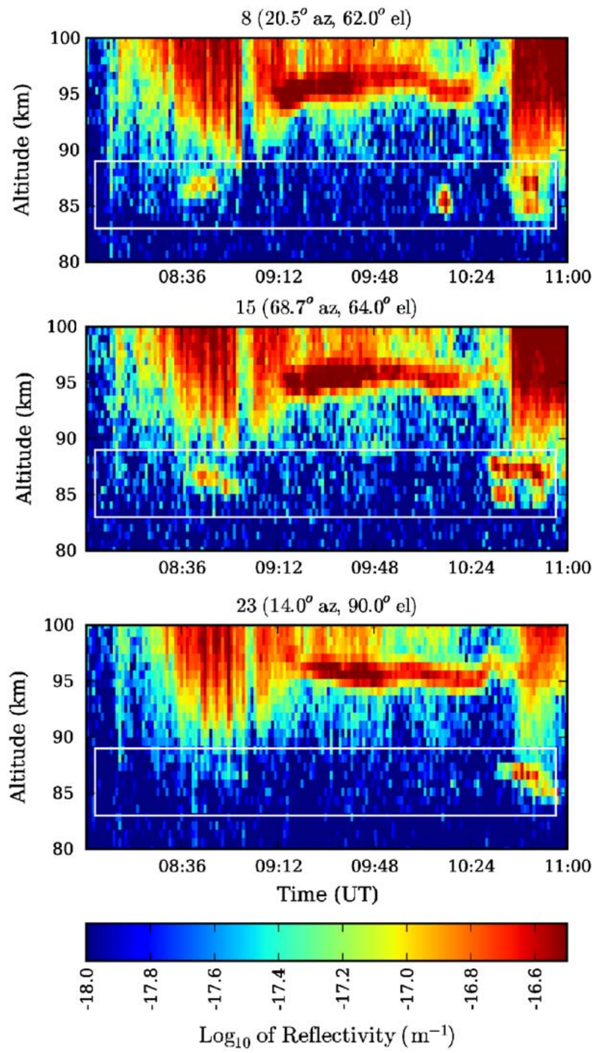

Fig. 6. Radar volume reflectivity plots for 3 of the 26 beams, 8, 15 and 23 (zenith) with positions indicated in Fig. 1. These plots are representative of the full radar dataset and reveal the presence of auroral precipitation, a sporadic E layer, and patchy PMSE structures. The white rectangle box isolates the region where PMSE were observed.

most prominent around 10:30 UT. By 11:00 UT (03:00 LT), the lidar signal had returned back to its original level (around 2.5×10^{-7} sr^{-1}), and the NLC had divided into two indistinct, wavy layers separated by ~1 km that persisted for at least the next hour, until measurements stopped at dawn.

Fig. 6 shows 3 examples of the PFISR measurements of radar reflectivity for this night extending over an ~5 h period from 06:00 to 11:00 UT. The plots show the radar volume reflectivity for beams 8, 15, and 23. These positions correspond to due north of the radar bore-sight direction (beam 8), to the east side of the radar field (beam 15) and zenith (beam 23) as indicated in Fig. 1. The data were averaged for ~1 min, and are presented as the $\log_{10}$ of radar-scattering cross-section per unit volume (i.e. the volume reflectivity), as a function of time and altitude (80–100 km). Absolute calibration of the radar backscatter was performed using the same analysis procedure as outlined by Nicolls et al. (2007). The color limits span the reflectivity range 10^{-18}–$10^{-16.8}$ m^{-1} and the derived reflectivity is accurate to within ~20%.

These plots are representative of the 26 individual beam measurements during this night and reveal the presence of auroral precipitation, a sporadic E layer, and patchy PMSE structures. Above 90 km, the reflectivity enhancements are due to ionization by variable (but large-scale) auroral precipitation. A well-defined sporadic E layer also formed at ~95 km altitude between ~09:10 and ~10:30 UT, indicating the presence of ionized heavy metallic ions. The PMSE occurred well below this level and revealed three isolated patches of structure, identified within the white box, which spans the altitude range of 83–88 km. PMSE were first detected around 08:40 UT, in the northern and eastern half of the radar array (as shown in beams 8 and 15). This coincided with the southward penetration of the visible NLC into the field of view of the radar array, but was not yet prominent in the zenith at PFRR (as indicated by the lack of PMSE signal in beam 23). A second patch of PMSE structure occurred at ~10:15 UT and is only evident in data from beam 8 in Fig. 5. This well-defined feature was detected over a limited azimuth range centered on the radar bore-sight (beams 3, 8, and 13) and its spatial characteristics are compared later with the visual NLC structures. The third patch of PMSE comprised stronger, intermittent echoes, that developed from ~10:30 to 11:00 UT, when the broad luminous NLC band approached and entered the PFISR/lidar sample volume. This feature was detected in all 26 beams indicating its relatively large spatial extent but again was strongest in the eastern half of the radar field. Around this time, strong auroral precipitation also occurred complicating the identification of this PMSE event. However, examination of the radar data show that the PMSE began several minutes earlier than the intense precipitation in many of the radar beams as illustrated in beam 15 and 23 data. As discussed in Nicolls et al. (2007, 2009), the observed intermittent temporal behavior of the PMSE detected by PFISR are quite consistent with other (limited) UHF observations of PMSE (e.g. Röttger et al., 1990; Hall and Röttger, 2001; La Hoz et al., 2006; Rapp et al., 2008).

4. Discussion

This investigation so far has established the presence of a well-defined NLC layer that was characterized by a broad luminous band containing a variety of NLC structures moving southwards towards and then over PFRR when it was detected by the Rayleigh lidar and the PFISR, which recorded strong, but intermittent PMSE structures. Before comparing the PMSE structures with the optical NLC data recorded by the imager and lidar, we first discuss the conditions necessary for observing PMSE. As already mentioned, PMSE requires turbulence, charged ice particles, and a sufficient gradient in the refractive index, which depends on the background electron number density and its gradient (e.g., Rapp et al., 2008). The absence of any one of these requirements can result in no detectable PMSE. At the small Bragg scales to which PFISR is sensitive (33 cm), these quantities must be particularly enhanced. The presence of large charged ice particles will extend the dissipation scale of the turbulence by enhancing the Schmidt number (which is proportional to the square of the ice particle radius). While spatial variability in ionization can lead to variability in intensity/occurrence of PMSE, there is evidence here that sufficient ionization was present for the detection of PMSE over the entire radar field of view. This evidence is in the coherent motion of PMSE through the radar field of view that was readily observed in movies (not shown), and has been previously discussed by Nicolls et al. (2007) (albeit for the daytime, solar-induced ionization), as well as in the appearance of PMSE before indications of strong auroral ionization. Furthermore, PMSE were not isolated to the times of intense particle precipitation (see Fig. 6). Therefore, it seems likely that sufficient ionization existed throughout the observation period owing to the persistent auroral precipitation, which occurred over a wide area encompassing the entire radar field of view. This will be discussed further when considering spatial structure in the PMSE data of Figs. 9 and 10.

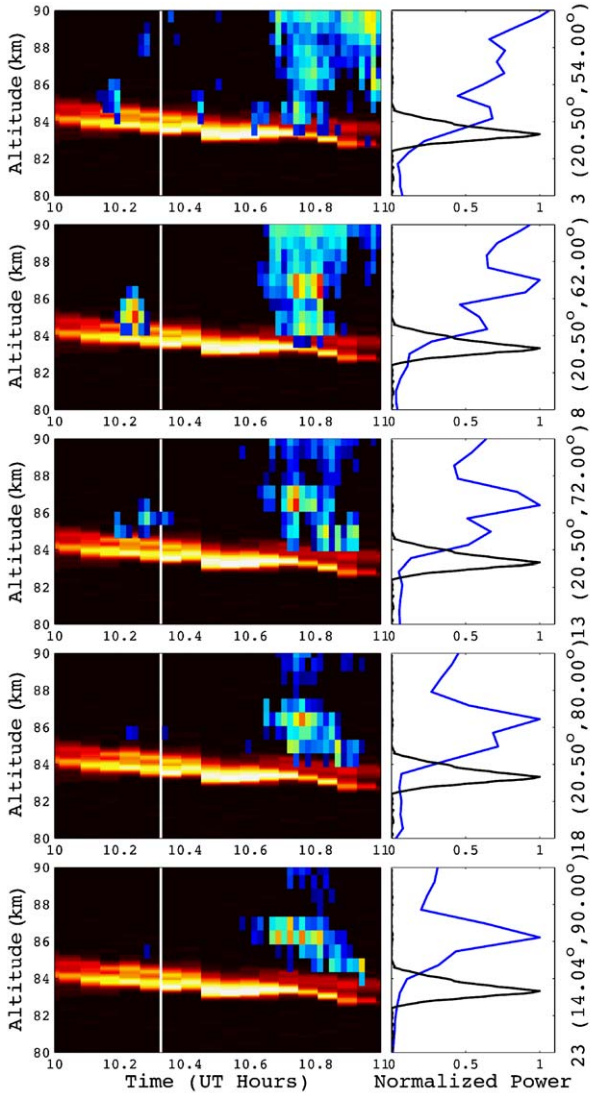

Fig. 7. Comparison of the Rayleigh lidar backscatter data with coincident measurements of radar reflectivity using data from the central (boresighted) row of PFISR's radar beams 3, 8, 13, 18 and 23 (zenith) as shown in Fig. 1. The data are plotted for the active period 10:00–11:00 UT. The altitude profiles to the right of each plot indicate the normalized power for the NLC layer and the PMSE from 10:36 to 10:48 UT when the strongest PMSE occurred.

Fig. 7 combines the Rayleigh lidar backscatter data with coincident measurements of radar reflectivity using data from the central (boresighted) row of PFISR's radar beams comprising beams 3, 8, 13, 18, and 23 (zenith) as shown in Fig. 1. Each plot compares the zenith lidar data with the PMSE structures as measured by these five beams. The data are plotted over the altitude range 80–90 km, for a 1 h period from 10:00 to 11:00 UT, when the lidar backscatter signal became significantly enhanced and strong PMSE were detected. The altitude profiles to the right of each plot indicate the normalized power for the NLC layer and the PMSE from 10:36 to 10:48 UT when the strongest PMSE occurred. These plots are representative of the full array of radar measurements and clearly show that the PMSE occurred mainly above the NLC layer, but occasionally extended down to coincide with the NLC. In particular, the isolated burst of PMSE that occurred around 10:15 UT in the northernmost beams (strongest in beam 8), appeared to penetrate well into the NLC layer, providing an excellent opportunity for directly comparing the 2-D PMSE and NLC structures. In contrast, the more extensive burst of PMSE observed from 10:30 to 11:00 UT enables us to investigate the PMSE structures residing mainly above the NLC layer and any association with auroral precipitation.

The 3-D development of the PMSE structures during this ~1-h period is summarized in Fig. 8. This figure is similar in its format to Fig. 3 of Nicolls et al. (2007). The radar data were integrated over 2 min intervals to obtain a time series of 2-D PMSE data plotted in 5 layers centered at 81.5, 83.0, 84.5, 86.0 and 87.5 km. The PMSE exhibited considerable altitude as well as spatial–temporal variations during this time (signal range-smeared over 1.5 km). These "stack" plots show the altitudinal structure in the PMSE during the two bursts of activity centered on ~10:15 and 10:45 UT. Initially the PMSE were relatively weak and featureless, but around 10:11 UT a prominent "finger-like" structure appeared to intrude from the north into the radar sample volume where it temporally brightened before fading over of a period of ~10 min. This feature was evident in the 84.5 and 86 km level data and extended over a zonal distance covered by only 1–2 beams. As already mentioned, this event occurred in association with visible NLC structures first entering radar volume from the north and is discussed in detail below (see Fig. 9). Strong, patchy PMSE features then developed, mainly to the north and east starting around 10:30 UT, rapidly brightening and expanding across the entire radar field of view. Initially, these PMSE were detected at the higher levels but quickly penetrated down to 84.5 km level

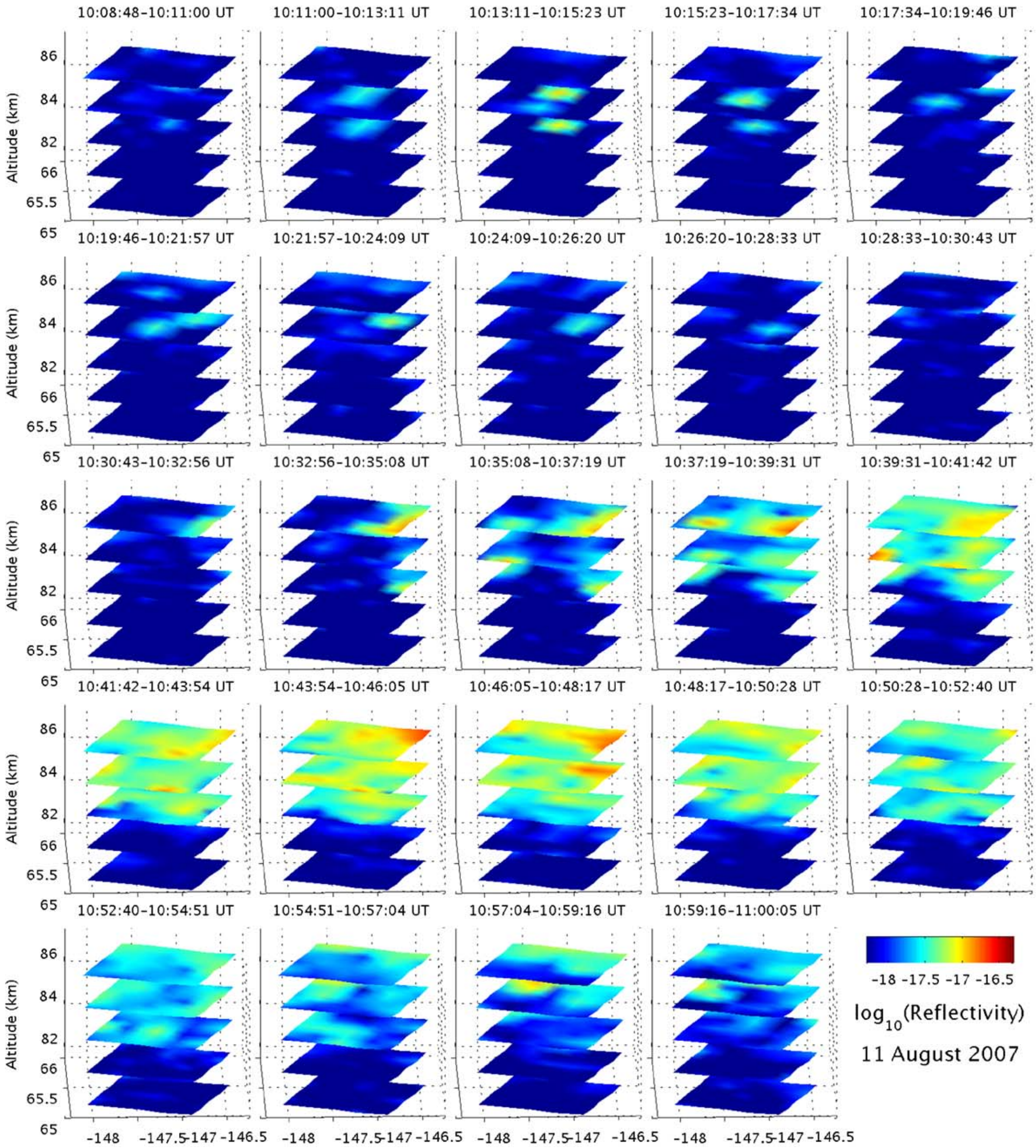

Fig. 8. Three-dimensional plots showing the altitudinal and spatial variation of PMSE for the same period as Fig. 7. The radar data were integrated over 2 min intervals to obtain a time series of 2-D PMSE data plotted in 5 layers centered at 81.5, 83.0, 84.5, 86.0 and 87.5 km. These "stacks" show the altitudinal structure in the PMSE during the two bursts of activity centered on ~10:15 and 10:45 UT.

located just above the NLC layer as indicated by the lidar data of Figs. 5 and 7. This situation prevailed for ~20 min until ~10:55 UT when the PMSE weakened and subsequently were detected only at the higher levels. During this event, the integrated radar reflectivity over 82–87 km increased by two orders of magnitude. At 11:00 UT, the radar was switched to a spectral observing mode where the PMSE echoes were observed to fade rapidly. Spectral measurements continued through dawn for the next 8 h and bursts of PMSE were again recorded a few hours later, centered around 14:00 and 17:45 UT (Nicolls et al., 2009).

The similarity between the 2-D PMSE and visible NLC structures observed during the 1-h period (10:00–11:00 UT) prior to dawn twilight is examined in Figs. 9 and 10, which focus on the two periods of strong PMSE activity discussed in Fig. 7. Fig. 9a shows a geographic map of the NLC display imaged from Gerstle River at 10:15 UT when the isolated "finger-like" PMSE structure was observed. At this time, an elongated wave crest is evident extending ahead of the broad NLC band and into the radar sample volume (indicated by the white box). This structure is clearly evident in Fig. 9b, which shows an enlarged image of the NLC data encompassing the radar common volume. The "finger-like" NLC structure is evidence at the top of the box extending southwards well into the radar field of view. The clusters of small bright patches in the right side of the image are due to meteorological cloud. Fig. 9c shows the corresponding PMSE data at 10:15 UT from 83.0 to 87.5 km. These were characterized by a single elongated feature apparently extending from the northern edge of the radar field towards its center. The similarity between the 2-D NLC and PMSE structures is striking, given their different measurement techniques and their different spatial resolutions.

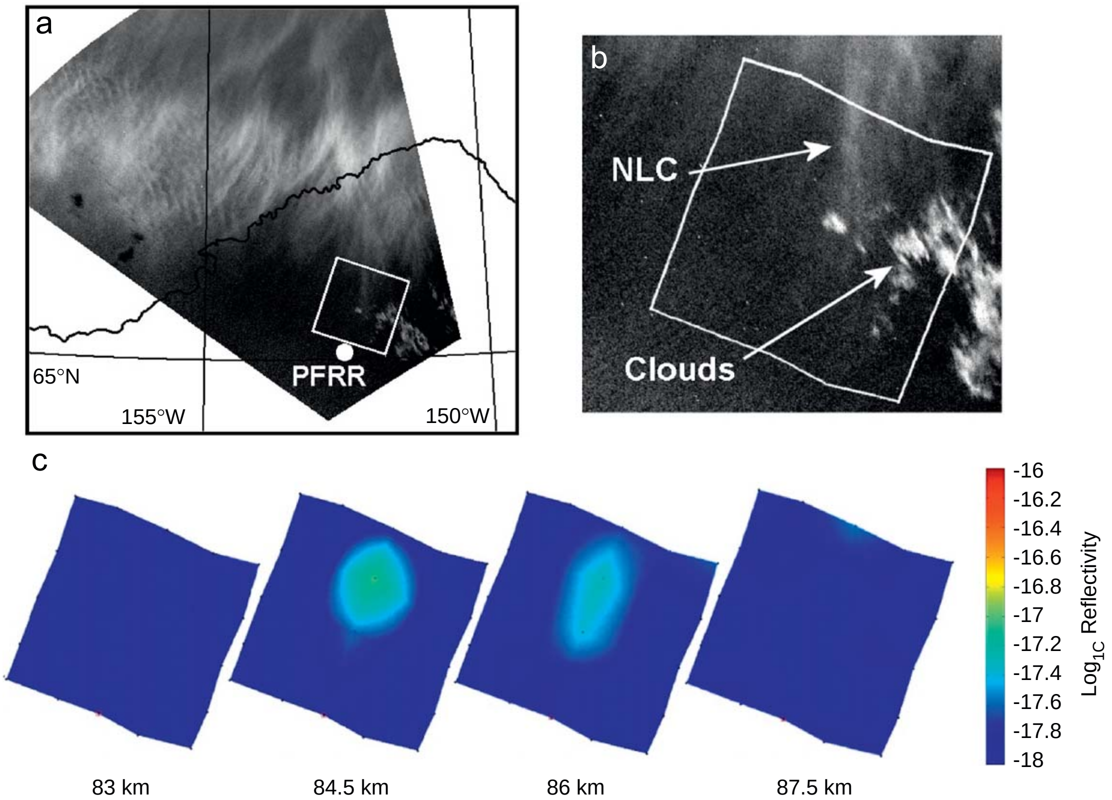

Fig. 9. Comparison of NLC and PMSE structures observed around 10:15 UT. Panel (a) shows a geographic map of the NLC display imaged from Gerstle River. An elongated wave crest extended ahead of the broad NLC band into the radar sample volume (indicated by the white box). (b) An enlarged image of the NLC data encompassing the radar common volume showing the ''finger-like'' NLC structure. The clusters of small bright patches in the right side of the image are due to meteorological cloud. Panel (c) shows the corresponding PMSE data at 10:15 UT from 83.0 to 87.5 km when a similar ''finger-like'' PMSE structure was observed coincident with the NLC layer.

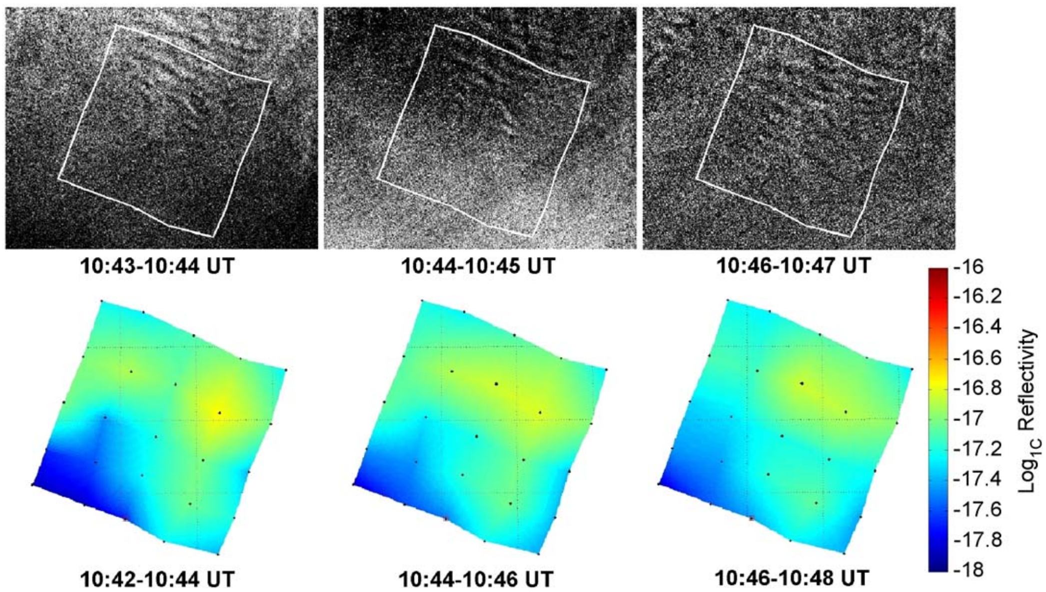

Fig. 10. Comparison of visible NLC structures (upper panel) and corresponding PMSE structures at 84.5 km level (lower panel). The difference images were obtained by subtracting two consecutive photographs recorded at 30 s intervals and show a series of billow structures with horizontal wavelength of 4.9 ± 0.2 km entering the radar field of view from the north (propagation azimuth of 207°N). The lower panel shows the corresponding 2-D PMSE maps, revealing clear evidence of elongated PMSE structures of similar location and orientation to the NLC billows.

Furthermore, the PMSE structures were limited in altitude to the 84.5–86.0 km range, which coincided well with the NLC layer as determined by lidar (Fig. 7) suggesting that these radar and optical structures are of related origin.

Fig. 10 shows a second comparative example focusing on the very active period ~10:42–10:48 UT when PMSE penetrated down to the topside of the NLC layer. The upper part of this figure shows three example images of NLC taken during this period showing the presents of billow-type wave structure in the radar sample area. These are difference images obtained by subtracting two consecutive photographs recorded at 30 s intervals. This is a technique often used in airglow studies to enhance faint wave structure (e.g., Li et al., 2005; Hecht et al., 2005). In this case, the billows are clearly resolved against the increasing twilight foreground (SDA$\approx$10°). These three images show a series of billow structures with horizontal wavelength of 4.9 ± 0.2 km entering the radar field of view from the north (propagation azimuth of 207°N). The lower plots in Fig. 10 show the corresponding 2-D PMSE maps centered at 84.5 km. Each map shows clear evidence of elongated PMSE structures to the north that appear well aligned (in an east–west sense) with the radar volume. Again, the comparison between the NLC billow structures and the lower spatial resolution radar PMSE signatures is striking.

To summarize, these are the first 2-D comparisons of PMSE and visible NLC structure over the same height range. Although previous lidar and radar measurements have often revealed strong correlations in the temporal variability of PMSE and NLC, especially when they occur in close proximity to each other (e.g., Nussbaumer et al., 1996; She et al., 2006; Gerding et al., 2007), our new 2-D observations suggest similar horizontal structuring and orientation of the common volume PMSE and NLC features (but the NLC data have finer resolution due to the limited number of beams employed by PFISR for this experiment). Furthermore, movies of the radar reflectivity data strongly suggest that the enhanced PMSE features moved into the field of view from the north, which qualitatively agrees very well with the observed motion of the NLC structures from the image data. As structure in ground-based NLC images results from the strong forward scattering of sun light mainly from ice particles located near the base of the NLC layer (Gadsden and Schröder, 1989), this study shows that it was important to compare the PMSE and NLC over the same altitude range. On this occasion, the lidar data indicated that the NLC base varied from 83 to 84.5 km during the night.

These observations are limited and may have been fortuitous, but the good agreement between the 2-D PMSE data and the NLC imagery is not unexpected as they both have common sources arising from the NLC ice particles (probably of different sizes) causing the optical and radar scattering. Although the origins of the PMSE and NLC signals are different, it is reasonable to expect correlations in their motion and in scale sizes when the signals are compared over a common height range. This statement is valid as long as the PMSE structures acquire long enough diffusion times to become embedded in the background winds, which indeed seems to be the case, as suggested by Nicolls et al. (2009) using spectral measurements of PMSE obtained immediately following these measurements.

Alternatively, it is possible that some of the observed intermittency in the PMSE and in particular their spatial 2-D structures (as shown in Figs. 9 and 10) is due to variations in the background ionization. As discussed earlier, these observations occurred together with auroral particle precipitation, which enhanced the otherwise low nighttime D-region ionization. Examples of the altitudinal and temporal variability of the auroral ionization as determined by the radar reflectivity measurements for 3 of the 26 beams are presented in Fig. 6. These data show that the spatially localized burst of PMSE that occurred around 10:15 UT were clearly not connected with direct penetration of auroral electrons. Therefore, the good agreement between the visible NLC and PMSE structures around 85 km (shown in Fig. 9) is almost certainly not due to variability induced by the auroral ionization, the effects of which were confined to altitudes >93 km during this event. In contrast, the PMSE measurements from $\sim$10:30 UT occurred at about the same time as strong auroral ionization extended down to at least the 90 km level, making it harder to discriminate between the auroral ionization signature and the upper levels of the PMSE structures. Furthermore, the time series of the radar reflectivity "stack" plots, presented in Fig. 8 show that strong PMSE structures occurred first at the upper levels and then penetrated down towards the NLC layer. It is therefore possible that the observed 2-D structure in the radar reflectivity shown in Fig. 10 may have been due, at least in part, to auroral ionization. However, close inspection of the zenith data presented in Fig. 6 (beam 23) clearly shows that PMSE structures occurred several minutes prior to the onset of the strong auroral precipitation. The same situation was observed in data from several other beams at this time. This fact, together with the striking agreement between the elongated PMSE structures shown in Fig. 10 and the associated NLC billows, suggests that auroral ionization was not a key factor in the observed 2-D PMSE structures. Thus, while we recognize that some PMSE variability was due to background parameters, such as the level of ionization, the observed small-scale spatial variability in the PMSE structures was most probably due to the advection of fossilized structures. These were formed in regions where the turbulence energy dissipation rates and Schmidt numbers (controlled mainly by the presence of the large charged ice particles) were sufficiently enhanced.

We now discuss the possible origin of the strong, intermittent PMSE observed on this night. To date, most measurements of PMSE have been made at VHF frequencies around 50 MHz. Detailed investigations of their Doppler spectra indicate a clear association with the occurrence of neutral turbulence in combination with the presence of charged ice particles in the polar upper mesosphere, which act to extend the electron density irregularity spectrum, enabling their detection by radar due to the significantly enhanced Schmidt number (e.g., Kelley et al., 1987; Lübken et al., 1993). This said, Lübken et al. (2002) presented a detailed comparison of in-situ rocket measurements of upper mesospheric neutral air turbulence simultaneous with collocated radar measurements of PMSE. Although their observations agreed with the current consensus that PMSE are closely related to charged ice particles, they also concluded that neutral air turbulence played only a minor role in the creation of PMSE. Most recently, Rapp et al. (2008) have investigated PMSE measured at three frequencies using Northern European radars operating at 53.5, 224, and 930 MHz. Their findings strongly support the current standard theory that the PMSE, as measured at a range of VHF and UHF frequencies, are created by turbulent scatter in the presences of large Schmidt numbers >2500. In concert with these results, Næsheim et al. (2008) have also shown that at UHF where the Bragg scattering wavelengths are smallest, PMSE are only observed when there is ongoing strong turbulence and are normally confined to the lower part of the VHF PMSE layer, where the largest ice particles are expected in close proximity of the visible NLC layer.

Possible sources of the turbulence are Kelvin–Helmholtz instabilities generated by strong wind shears or gravity wave breaking in the upper mesosphere. Hill et al. (1999) have modeled turbulence induced fluctuations in ionization and their effects on PMSE. Their analysis showed the temporal evolution of a turbulence layer initiated by Kelvin–Helmholtz instability. Furthermore, comparison with VHF signal to noise measurements at 50 MHz supported the hypothesis that massive ions (charged ice particles) mixed within this turbulence layer is a reasonable mechanism for the generation of PMSE layers. Building on these results, Fritts et al. (2003) have discussed the layering phenomena due to turbulence associated with shear instabilities and gravity wave breaking. They showed that the local effects of turbulence due to Kelvin–Helmholtz instability are expected to persist much longer than those due to gravity wave breaking as the shear instabilities cause turbulence mixing confined by stratification to a narrow (typically 1 km wide) layer, whereas gravity wave breaking results in turbulence activity that is expected to progress with the phase of the wave. Moreover, they discussed the importance of persistent, thin laminae that develop at the edges of the turbulent region where sharp gradients in temperature occur (Coulman et al., 1995), which could affect the NLC structures.

Turning now to our coordinated measurements on this night, the image data presented herein (Figs. 3, 4, 9 and 10) clearly show the evolution of the broad luminous NLC band as it passed overhead at PFRR and the development of an extensive "sea" of small-scale billow structures covering a large fraction of the camera's field of view. These billows were observed to form around 10:00 UT and to persist for more than 1 h in the zenith sky, until dawn twilight (12:15 UT, SDA $\sim 6°$). Billow wave patterns are frequently observed in NLC and have been associated with Kelvin–Helmholz instabilities that are generated by strong wind shears near the summer mesospause (e.g., Fogle and Haurwitz, 1969; Fritts et al., 1993). On this occasion, the presence of such an extensive billow wave field provides convincing evidence for the existence of a strong and persistence wind shear (typically >40 m/s/km) at NLC heights, and its subsequent association with the development of a layer of neutral turbulence initiated by the Kelvin–Helmholz instability mechanism. Further evidence in support of the generation of neutral turbulence layer is found in the coincident lidar measurements which detected a well-developed NLC layer of ~ 1 km thickness that varied in height during the night from ~ 83 to 85.5 km, as shown in Fig. 5. After 10:00 UT, these data reveal evidence for stronger backscatter signals at the upper and lower boundary of the NLC layer, which later developed into two faint NLC layers (after ~ 11:00 UT) separated by ~ 1 km that persisted until the lidar measurements terminated at 12:15 UT. The formation of such a double-layer NLC structure may be a signature of the development of laminae at the edges of a turbulent layer induced by Kelvin–Helmholz instability as discussed by Fritts et al. (2003). Thus, it is possible that the occurrence of strong neutral turbulence associated with the billows, together with the presence of large charged NLC ice particles, were the source of the strong, intermittent PMSE observed by the radar during this time. This result is further compounded by the recent PMSE study of Nicolls et al. (2009) using data obtained immediately following these observations. They concluded that neutral turbulence together with enhanced Schmidt number in the presence of charged ice could indeed explain the observations of the PMSE structures measured at 450 MHz on this occasion.

5. Summary

This paper describes coincident 3-D radar, lidar and optical image measurements of dynamical structures in PMSE and NLC as recorded from central Alaska on 10/11 August 2007. During this night, a well-defined NLC display that was characterized by a large luminous band containing a variety of NLC wave structures was observed to move towards and over PFRR at the same time that strong but intermittent PMSE measurements were recorded by PFISR enabling the first detailed investigation of the occurrence and horizontal spatial structures of NLC and PMSE, over a limited ~ 2 h period. Two PMSE events were investigated in detail: the first was an isolated burst of PMSE structure that occurred over a limited altitude range ~ 2 km (84–86 km), penetrating into the upper part of the NLC layer, and well below the auroral precipitation region, the second event was of longer duration and occurred mainly above the NLC layer in the presence of auroral particle precipitation. Using the lidar data to determine the NLC layer altitude, direct comparison of the optical NLC imagery with the 2-D radar PMSE signatures revealed striking similarities in the location and orientation of the observed NLC and PMSE structures (within the current resolution of the radar measurements), suggesting a direct link. Furthermore, the NLC and PMSE structures appeared to move in the same direction (southward) on this occasion.

This was an unusual NLC display producing strong lidar and radar echoes at the time when extensive, small-scale (4.9 km) billow waves were observed to develop. Together these results support the theory that strong shearing responsible for the billows may have played a key role in the development of neutral turbulence via the Kelvin–Helmholz mechanism resulting in the intense intermittent PMSE in close proximity to the NLC layer. This exploratory study has established the capability for in-depth probing of the NLC and PMSE fields now in 2-D and 3-D to investigate their relationships and dynamical variability. Our (limited) results are suggestive of a one-to-one correlation in NLC and PMSE structure, but clearly more observations with increased spatial resolution are needed to establish their common volume properties.

Acknowledgements

These ground-based optical and radar measurements were made in coordination with the NASA AIM mission. The NLC image observations were supported by a sub-contract from Hampton University to Utah State University. The PFISR was developed under an NSF cooperative agreement Grant ATM-0121483 and the radar data collection and analysis was supported under Grant ATM-0608577. The lidar observations were conducted in cooperation with the National Science Foundation Research Experience for Undergraduates Program and the Polar Aeronomy and Radio Science (PARS) Summer School. The NICT Rayleigh lidar is operated as part of the Alaska Project. Poker Flat Research Range is a rocket range operated by the Geophysical Institute of the University of Alaska Fairbanks with support from NASA. We thank the Poker Flat Research Range staff for their technical support and assistance in these joint measurements. One of us (JBT) was partially supported by the PARS 2007 summer workshop.

References

Backhouse, T.W., 1885. The luminous cirrus cloud of June and July. The Meteorological Magazine 20, 133.

Bailey, S.M., Merkel, A.W., Thomas, G.E., Carstens, J.N., 2005. Observations of polar mesospheric clouds by the student nitric oxide explorer. Journal of Geophysical Research 100, D13203.

Balsley, B.B., Ecklund, W.L., Fritts, D.C., 1983. VHF echoes from the high-latitude mesosphere and lower thermosphere: observations and interpretations. Journal of Atmospheric Sciences 40, 2451–2466.

Bjorn, L.G., Kopp, E., Herrmann, U., Eberhardt, P., Dickinson, P.H.G., Mackinnon, D.J., Arnold, F., Witt, G., Ludin, A., Jenkins, D.B., 1985. Heavy ionospheric ions in the formation process of noctilucent clouds. Journal of Geophysical Research 90, 7985–7998.

Carbary, J.F., Morrison, D., Romick, G.J., 2000. Transpolar structure of polar mesospheric clouds. Journal of Geophysical Research 105, 24,763–24,769.

Chilson, P.B., Kirkwood, S., Haggstrom, L., 2001. Frequency domain interferometry mode observations of PMSE using the EISCAT VHF radar. Annales Geophysicae 18, 1599–1612.

Chilson, P.B., Yu, T.-Y., Palmer, R.D., Kirkwood, S., 2002. Aspect sensitivity measurements of polar mesosphere summer echoes using coherent radar imaging. Annales Geophysicae 20, 213–223.

Cho, J.Y.N., Kelley, M.C., 1992. Enhancement of Thomson scatter by charged aerosols in the polar mesosphere: measurements with a 1.29-GHz radar. Geophysical Research Letters 19, 1097–1100.

Cho, J.Y.N., Röttger, J., 1997. An updated review of polar mesosphere summer echoes: observation, theory, and their relationship to noctilucent clouds and subvisible aerosols. Journal of Geophysical Research 102, 2001–2020.

Cho, J.Y.N., Hall, T.M., Kelly, M.C., 1992. On the role of charged aerosols in polar mesosphere summer echoes. Journal of Geophysical Research 97, 875–886.

Chu, X., Gardner, C.S., Pappen, G., 2001. Lidar observations of polar mesospheric clouds at the South Pole: diurnal variations. Geophysical Research Letters 26, 1937–1940.

Collins, R.L., Kelley, M.C., Nicolls, M.J., Ramos, C., Hou, T., Stern, T.E., Mizutani, K., Itabe, T., 2003. Simultaneous lidar observations of a noctilucent cloud and an internal wave in the polar mesosphere. Journal of Geophysical Research 108 (D8), 8435.

Collins, R.L., Taylor, M.J., Nielsen, K., Mizutani, K., Murayama, Y., Sakanoi, K., DeLand, M., 2009. Noctilucent cloud in the Western Arctic in 2005: simultaneous lidar and camera observations and analysis. Journal of Atmospheric and Solar-Terrestrial Physics, in press, doi:10.1016/j.jastp.2008.09.044.

Coulman, C.E., Vernin, J., Fuchs, A., 1995. Optical seeing-mechanism of formation of thin turbulent laminae in the atmosphere. Applied Optics 34, 5461–5474.

Czechowsky, P., Ruster, R., 1997. VHF radar observations of turbulent structures in the polar mesopause region. Annales Geophysicae 15, 1028–1036.

Czechowsky, P., Ruster, R., Schmidt, G., 1979. Variations of mesospheric structures in different seasons. Geophysical Research Letters 6, 459–462.

Czechowsky, P., Reid, I.M., Ruster, R., 1988. VHF radar measurements of the aspect sensitivity of the summer polar mesopause echoes over Andenes (69°N, 16°E), Norway. Geophysical Research Letters 15, 1259–1262.

Deland, M.T., Shettle, E.P., Thomas, G.E., Olivero, J.J., 2006. A quarter-century of satellite polar mesospheric cloud observations. Journal of Atmospheric and Solar-Terrestrial Physics 68, 9–29.

Donahue, T.M., Guenther, B., Blamont, J.E., 1972. Noctilucent clouds in daytime: circumpolar particulate layers near the summer mesopause. Journal of Atmospheric Science 29, 1205.

Ecklund, W.L., Balsley, B.B., 1981. Long-term observations of the arctic mesosphere with the MST radar at Poker Flat, Alaska. Journal of Geophysical Research 86, 7775–7780.

Evans, W.F.J., Laframboise, L.R., Sine, K.R., Wiens, R.H., Shepherd, G.G., 1995. Observation of polar mesospheric clouds in summer, 1993 by the WINDII instrument on UARS. Geophysical Research Letters 22, 793–2796.

Fiedler, J., Baumgarten, G., von Cossart, G., 2005. Mean diurnal variations of noctilucent clouds during 7 years of lidar observations at ALOMAR. Annales Geophysicae 23, 1–7.

Fogle, B., Haurwitz, B., 1969. Wave forms in noctilucent clouds. Deep-Sea Research 16, 85–95.

Fritts, D.C., Alexander, M.J., 2003. Gravity wave dynamics and effects in the middle atmosphere. Review of Geophysics 41 (1), 1003.

Fritts, D.C., Isler, J.R., Thomas, G.E., Andreassen, Ø., 1993. Wave breaking signatures in noctilucent clouds. Geophysical Research Letters 20, 2039–2042.

Fritts, D.C., Bizon, C., Werne, J.A., Meyer, C.K., 2003. Layering accompanying turbulence generation due to shear instability and gravity-wave braking. Journal of Geophysical Research 108.

Gadsden, M., 1981. The silver-blue cloudlets again: nucleation and growth of ice in the mesosphere. Planet and Space Science 29, 1079–1087.

Gadsden, M., 1998. The North-West Europe data on noctilucent clouds: a survey. Journal of Atmospheric and Solar-Terrestrial Physics 60, 1163–1174.

Gadsden, M., Schröder, W., 1989. Noctilucent Clouds. Springer, Berlin.

Gadsden, M., Taylor, M.J., 1994. Anweisungen für die photographischen aufnahmen der leuchtenden nachtwolken—103 years on. Journal of Atmospheric and Terrestrial Physics 56, 447–459.

Gerding, M., Höffner, J., Rauthe, M., Singer, W., Zecha, M., Lübken, F.-J., 2007. Simultaneous observation of noctilucent clouds, mesospheric summer echoes, and temperature at a midlatitude station (54°N). Journal of Geophysical Research 112.

Grahn, S., Witt, G., 1971. Rep AP-4 Inst Meteorol. University of Stockholm.

Hall, C.M., Röttger, J., 2001. Initial observations of polar mesospheric summer echoes using the EISCAT SVALBARD radar. Geophysical Research Letters 28, 131–134.

Hansen, G., Serwazi, M., von Zahn, U., 1989. First detection of a noctilucent cloud by lidar. Geophysical Research Letters 16, 1445–1448.

Hecht, J.H., Liu, A.Z., Waltrescheid, R.L., Rudy, r.J., 2005. Maui mesosphere and lower thermosphere (Maui MALT) observations of the evolution of Kelvin--Helmholtz billows formed near 86 km altitude. Journal of Geophysical Research 110.

Hill, R.J., Gibson-Wilde, D.E., Werne, J.A., Fritts, D.C., 1999. Turbulence-induced fluctuations in ionization and application to PMSE. Earth Planets Space 51, 499–513.

Hoffmann, P., Singer, W., Bremer, J., 1999. Mean seasonal and diurnal variations of PMSE and winds from 4 years of radar observations at ALOMAR. Geophysical Research Letters 26, 1525–1528.

Hoffmann, P., Rapp, M., Serafimovich, A., Latteck, R., 2005. On the occurrence and formation of multiple layers of polar mesosphere summer echoes. Geophysical Research Letters 32.

Hoppe, U.-P., Hall, C., Röttger, J., 1988. First observations of summer polar mesospheric backscatter with a 224-MHz radar. Geophysical Research Letters 15, 28–31.

Janches, D., Fritts, D.C., Nicolls, M.J., Heinselman, C.J., 2009. Observations of D-region structure and atmospheric tides with PFISR during active aurora. Journal of Atmospheric and Solar-Terrestrial Physics, this issue, doi:10.1016/j.jastp.2008.08.015.

Jesse, O., 1896. Die Höhe der leuchtenden nachtwolken. Astronomische Nachrichten 140, 161–168.

Jensen, E.J., Thomas, G.E., 1988. A growth-sedimentation model of polar mesospheric clouds: comparison with SME measurements. Journal of Geophysical Research 93, 2461–2473.

Jensen, E.J., Thomas, G.E., Balsley, B.B., 1988. On the statistical correlation between polar mesospheric cloud occurrence and enhanced mesospheric radar echoes. Geophysical Research Letters 15, 315–318.

Kelley, M.C., Farley, D.T., Röttger, J., 1987. The effect of cluster ions on anomalous VHF backscatter from the summer polar mesosphere. Geophysical Research Letters 14, 1031–1034.

Kirkwood, S., Cho, J., Hall, C.M., Hoppe, U.-P., Murtagh, D.P., Stegman, J., Swartz, W.E., van Eyken, A.P., Wannberg, G., Witt, G., 1995. A comparison of PMSE and other ground-based observations during the NLC-91 campaign. Journal of Atmospheric and Terrestrial Physics 57, 35–44.

La Hoz, C., Havnes, O., Næsheim, L.I., Hysell, D.L., 2006. Observations and theories of polar mesospheric summer echoes at a Bragg wavelength of 16 cm. Journal of Geophysical Research 111, D04203.

Leslie, R., 1885. Sky glows. Nature 32, 245.

Li, F., Liu, A.Z., Swenson, G.R., Hecht, J.H., Robinson, W.A., 2005. Observations of gravity wave breakdown into ripples associated with dynamical instabilities. Journal of Geophysical Research 110.

Lübken, F.-J., 1999. Thermal structure of the Arctic summer mesosphere. Journal of Geophysical Research 104, 9135–9149.

Lübken, F.-J., Lehmacher, G., Blix, T., Hoppe, U.-P., Thrane, E., Cho, J., Swartz, W., 1993. First in-situ observations of neutral and plasma density fluctuations within a PMSE layer. Geophysical Research Letters 20, 2311–2314.

Lübken, F.-J., Fricke, K.-H., Langer, M., Hoffmann, P., Singer, W., Inhester, B., Witt, G., 1995. Simultaneous measurements of noctilucent clouds, polar mesosphere summer echoes, and the temperature near the mesospause. In: Proceedings of the 12th ESA Symposium on Rocket and Balloon Programmes and Related Research, ESA SP-370, 61-66, European Space Agency, Paris.

Lübken, F.-J., Rapp, M., Hoffmann, P., 2002. Neutral air turbulence and temperatures in the vicinity of polar mesosphere summer echoes. Journal of Geophysical Research 107.

Mizutani, K., Itabe, T., Yasui, M., Aoki, M., Murayama, Y., Collins, R.L., 2000. Rayleigh and Rayleigh Doppler lidars for the observations of the Arctic Middle Atmosphere. IEICE Transactions on Communications, E 83-B (9), 2004–2009.

Næsheim, L.I., Havnes, O., La Hoz, C., 2008. A comparison of polar mesosphere summer echo at VHF (224 MHz) and UHF (930 MHz) and the effects of artificial electron heating. Journal of Geophysical Research 113.

Nicolls, M.J., Heinselman, C.J., Hope, E.A., Ranjan, S., Kelley, M.C., Kelly, J.D., 2007. Imaging of polar mesosphere summer echoes with the 450 MHz Poker flat advanced modular incoherent scatter radar. Geophysical Research Letters 34, L20102.

Nicolls, M.J., Kelley, M.C., Varney, R.H., Heinselman, C.J., 2009. Spectral observations of polar mesospheric summer echoes at 33 cm (450 MHz) with the Poker Flat Incoherent Scatter Radar. Journal of Atmospheric Solar-Terrestrial Physics, this issue, doi:10.1016/j.jastp.2008.04.019.

Nussbaumer, V., Fricke, K.-H., Langer, M., Singer, W., von Zahn, U., 1996. First simultaneous and common-volume observations of NLC and PMSE by lidar and radar. Journal of Geophysical Research 101, 19,161–19,167.

Paton, J., 1964. Noctilucent clouds. Meteorological Magazine 93, 161–179.

Rapp, M., Lübken, F.-J., 2003. On the nature of PMSE: electron diffusion in the vicinity of charged particles revisited. Journal of Geophysical Research 108, 8437.

Rapp, M., Lübken, F.-J., 2004. Polar mesosphere summer echoes (PMSE): review of observations and current understanding. Atmospheric Chemistry and Physics 4, 2601–2633.

Rapp, M., Thomas, G.E., 2006. Modeling the microphysics of mesospheric ice particles: assessment of current capabilities and basic sensitivities. Journal of Atmospheric and Solar-Terrestrial Physics 68, 715–744.

Rapp, M., Gumbel, J., Lübken, F.-J., Latteck, R., 2002. D region electron number density limits for the existence of polar mesosphere summer echoes. Journal of Geophysical Research 107 (D14).

Rapp, M., Strelnikova, I., Latteck, R., Hoffman, P., Hoppe, U.-P., Haggstrom, I., Rietveld, M.T., 2008. Polar mesosphere summer echoes (PMSE) studied at Bragg wavelengths of 2.8 m, 67 cm, and 16 cm. Journal of Atmospheric and Solar-Terrestrial Physics 70, 947–961.

Röttger, J., La Hoz, C., 1990. Characteristics of polar mesosphere summer echoes (PMSE) observed with the EISCAT 224 MHz radar and possible explanations of their origin. Journal of Atmospheric Terrestrial Physics 52, 893–906.

Röttger, J., Rietveld, M.T., La Hoz, C., Hall, T., Kelley, M.C., Swartz, W.E., 1990. Polar mesosphere summer echoes observed with the EISCAT 933-MHz radar and the CUPRI 46.9-MHz radar, their similarity to 224-MHz radar echoes and their relation to turbulence and electron density profiles. Radio Sciences 25, 671–687.

Russell III, J.M., Bailey, S.M., Gordley, L.L., Rusch, D.W., Horányi, M., Hervig, M.E., Thomas, G.E., Randall, C.E., Siskind, D.E., Stevens, M.H., Summers, M.E., Taylor, M.J., Englert, C.R., Espy, P.J., McClintock, W.E., Merkel, A.W., 2009. The Aeronomy of Ice in the Mesosphere (AIM) mission: overview and early science results. Journal of Atmospheric Solar-Terrestrial Physics, in press, doi:10.1016/j.jastp.2008.08.011.

Ruster, R., 1997. High resolution measurements in the summer polar mesosphere. Geophysical Research Letters 24, 1115–1118.

Ruster, R., Czechowsky, P., Hoffmann, P., Singer, W., 1996. Gravity wave signatures at mesopause heights. Annales Geophysicae 14, 1186–1191.

She, C.Y., Williams, B.P., Höffmann, P., Latteck, R., Baumgarten, G., Vance, J.D., Fiedler, J., Acott, P., Fritts, D.C., Lübken, F.-J., 2006. Simultaneous observation of sodium atmos, NLC and PMSE in the summer mesopause region above ALOMAR, Norway (69°N, 12°E). Journal of Atmospheric and Terrestrial Physics 68, 93–101.

Strörmer, C., 1933. Height and velocity of luminous night clouds observed in Norway, 1932. Oslo University Publication 6, 1–45.

Tatarskii, U.I., 1961. Wave Propagation in a Turbulent Medium. McGraw-Hill Book Company, New York.

Taylor, M.J., Hapgood, M.A., Simmons, D.A.R., 1984. The effect of atmospheric screening of the visible border of noctilucent clouds. Journal of Atmospheric Terrestrial Physics 14, 865–869.

Taylor, M.J., van Eyken, A.P., Rishbeth, H., Witt, G., Witt, N., Clilverd, M.A., 1989. Simultaneous observations of noctilucent clouds and polar mesospheric radar echoes: evidence for noncorrelation. Planetary and Space Science 37, 1013–1020.

Taylor, M.J., Gadsden, M., Low, R.P., Zalcik, M.S., Brausch, J., 2002. Mesospheric cloud observations at unusually low latitudes. Journal of Atmospheric and Solar-Terrestrial Physics 64, 991–999.

Thayer, J.P., Rapp, M., Gerrard, A.J., Gudmundsson, E., Kane, T.J., 2003. Gravity-wave influences on Arctic mesospheric clouds as determined by a Rayleigh lidar at Sondrestrom, Greenland. Journal of Geophysical Research 108.

Thomas, G.E., 1984. Solar mesosphere explorer measurements of polar mesospheric clouds (noctilucent clouds). Journal of Atmospheric and Terrestrial Physics 46, 819–824.

Thomas, G.E., Olivero, J.J., Jensen, E.J., Schröder, W., Toon, O.B., 1989. Relation between increasing methane and the presence of ice clouds at the mesopause. Nature 338, 490–492.

Thomas, G.E., McPeters, R.D., Jensen, E.J., 1991. Satellite observations of polar mesospheric clouds by the solar backscattered ultraviolet spectral radiometer: evidence of a solar-cycle dependence. Journal of Geophysical Research 96, 927–939.

Varney, R.H., Nicolls, M.J., Heinselman, C.J., Kelley, M.C., 2009. Observations of polar mesospheric summer echoes using PFISR during the summer of 2007. Journal of Atmospheric Solar-Terrestrial Physics, in press, doi:10.1016/j.jastp.2009.01.002.

von Savigny, C., Burrows, J.P., 2007. Latitudinal variation of NLC particle radii derived from northern hemisphere SCIACHY/Envisat limb measurements. Advances in Space Research 40, 765–771.

von Zahn, U., 2003. Are noctilucent clouds truly a "miner's canary" of global change? Eos, Transactions, American Geophysical Union 84 (28), 261–268.

von Zahn, U., Bremer, J., 1999. Simultaneous and common-volume observations of noctilucent clouds and polar mesosphere summer echoes. Geophysical Research Letters 26, 1521–1524.

von Zahn, U., von Cossart, G., Fiedler, J., Rees, D., 1998. Tidal variations of noctilucent clouds measured at 69° latitude by ground based lidar. Geophysical Research Letters 25, 1289–1292.

Wickwar, V.B., Taylor, M.J., Herron, J.P., Martineau, B.A., 2002. Visual and lidar observations of noctilucent clouds above Logan, Utah, at 41.7°N. Journal of Geophysical Research 107.

Witt, G., 1962. Height, structure and displacements of noctilucent clouds. Tellus 14, 1–18.

Witt, G., Wilhelm, N., Stegman, J., Williams, A.P., Holback, B., Llewellyn, E., Pedersen, A., 1971. Rep AP-7 Inst Meteorol. University of Stockholm.

Zalcik, M.S., 1998. A possible increase in mid-latitude sightings of noctilucent clouds. Journal of the Royal Astronomical Society of Canada 92, 197–200.